The Astrophysical Journal Letters, 955:L8 (13pp), 2023 September 20 https://doi.org/10.3847/2041-8213/acf299

From Discovery to the First Month of the Type II Supernova 2023ixf: High and Variable Mass Loss in the Final Year before Explosion

Daichi Hiramatsu[1,2], Daichi Tsuna[3,4], Edo Berger[1,2], Koichi Itagaki[5], Jared A. Goldberg[6], Sebastian Gomez[7], Kishalay De[8,22], Griffin Hosseinzadeh[9], K. Azalee Bostroem[9,23], Peter J. Brown[10,11], Iair Arcavi[12], Allyson Bieryla[1], Peter K. Blanchard[13], Gilbert A. Esquerdo[1], Joseph Farah[14,15], D. Andrew Howell[14,15], Tatsuya Matsumoto[16], Curtis McCully[14,15], Megan Newsome[14,15], Estefania Padilla Gonzalez[14,15], Craig Pellegrino[14,15], Jaehyon Rhee[1,17], Giacomo Terreran[14,15], József Vinkó[18,19,20,21], and J. Craig Wheeler[18]

[1] Center for Astrophysics | Harvard & Smithsonian, 60 Garden Street, Cambridge, MA 02138-1516, USA; daichi.hiramatsu@cfa.harvard.edu
[2] The NSF AI Institute for Artificial Intelligence and Fundamental Interactions, USA
[3] TAPIR, Mailcode 350-17, California Institute of Technology, Pasadena, CA 91125-0001, USA
[4] Research Center for the Early Universe, School of Science, The University of Tokyo, 7-3-1 Hongo, Bunkyo-ku, Tokyo 113-0033, Japan
[5] Itagaki Astronomical Observatory, Yamagata 990-2492, Japan
[6] Center for Computational Astrophysics, Flatiron Institute, 162 5th Avenue, New York, NY 10010-5902, USA
[7] Space Telescope Science Institute, 3700 San Martin Drive, Baltimore, MD 21218-2410, USA
[8] MIT-Kavli Institute for Astrophysics and Space Research, 77 Massachusetts Ave., Cambridge, MA 02139, USA
[9] Steward Observatory, University of Arizona, 933 North Cherry Avenue, Tucson, AZ 85721-0065, USA
[10] Department of Physics and Astronomy, Texas A&M University, 4242 TAMU, College Station, TX 77843-4242, USA
[11] George P. and Cynthia Woods Mitchell Institute for Fundamental Physics & Astronomy, College Station, TX 77843, USA
[12] School of Physics and Astronomy, Tel Aviv University, Tel Aviv 69978, Israel
[13] Center for Interdisciplinary Exploration and Research in Astrophysics (CIERA) and Department of Physics and Astronomy, Northwestern University, 1800 Sherman Avenue, 8th Floor, Evanston, IL 60201, USA
[14] Las Cumbres Observatory, 6740 Cortona Drive, Suite 102, Goleta, CA 93117-5575, USA
[15] Department of Physics, University of California, Santa Barbara, CA 93106-9530, USA
[16] Department of Physics and Columbia Astrophysics Laboratory, Columbia University, Pupin Hall, New York, NY 10027, USA
[17] Department of Physics, Yonsei University, Seoul 03722, Republic of Korea
[18] University of Texas at Austin, 1 University Station C1400, Austin, TX 78712-0259, USA
[19] Konkoly Observatory, CSFK, MTA Center of Excellence, Konkoly-Thege M. út 15-17, Budapest, 1121, Hungary
[20] ELTE Eötvös Loránd University, Institute of Physics and Astronomy, Pázmány Péter sétány 1/A, Budapest, 1117 Hungary
[21] Department of Experimental Physics, University of Szeged, Dóm tér 9, Szeged, 6720, Hungary
Received 2023 July 6; revised 2023 August 17; accepted 2023 August 22; published 2023 September 19

Abstract

We present the discovery of the Type II supernova SN 2023ixf in M101 and follow-up photometric and spectroscopic observations, respectively, in the first month and week of its evolution. Our discovery was made within a day of estimated first light, and the following light curve is characterized by a rapid rise (≈5 days) to a luminous peak ($M_V \approx -18.2$ mag) and plateau ($M_V \approx -17.6$ mag) extending to 30 days with a fast decline rate of ≈0.03 mag day^{-1}. During the rising phase, $U-V$ color shows blueward evolution, followed by redward evolution in the plateau phase. Prominent flash features of hydrogen, helium, carbon, and nitrogen dominate the spectra up to ≈5 days after first light, with a transition to a higher ionization state in the first ≈2 days. Both the $U-V$ color and flash ionization states suggest a rise in the temperature, indicative of a delayed shock breakout inside dense circumstellar material (CSM). From the timescales of CSM interaction, we estimate its compact radial extent of $\sim(3\text{–}7)\times10^{14}$ cm. We then construct numerical light-curve models based on both continuous and eruptive mass-loss scenarios shortly before explosion. For the continuous mass-loss scenario, we infer a range of mass-loss history with 0.1–1.0 $M_\odot$ yr^{-1} in the final 2−1 yr before explosion, with a potentially decreasing mass loss of 0.01–0.1 $M_\odot$ yr^{-1} in ∼0.7–0.4 yr toward the explosion. For the eruptive mass-loss scenario, we favor eruptions releasing 0.3–1 $M_\odot$ of the envelope at about a year before explosion, which result in CSM with mass and extent similar to the continuous scenario. We discuss the implications of the available multiwavelength constraints obtained thus far on the progenitor candidate and SN 2023ixf to our variable CSM models.

Unified Astronomy Thesaurus concepts: Supernovae (1668); Core-collapse supernovae (304); Type II supernovae (1731); Massive stars (732); Red supergiant stars (1375); Stellar mass loss (1613); Circumstellar matter (241); Supergiant stars (1661)

Supporting material: data behind figures

1. Introduction

The majority of massive stars (zero-age main-sequence (ZAMS) masses of $M_{\rm ZAMS} \approx 8\text{–}25\,M_\odot$) end their lives when their iron cores collapse, leading to explosions as hydrogen-rich (H-rich) Type II supernovae (SNe II; see, e.g., Smartt 2009, 2015; Arcavi 2017, for reviews). While there is consensus that the progenitors of SNe II are red supergiants

[22] NASA Einstein Fellow.
[23] LSSTC Catalyst Fellow.

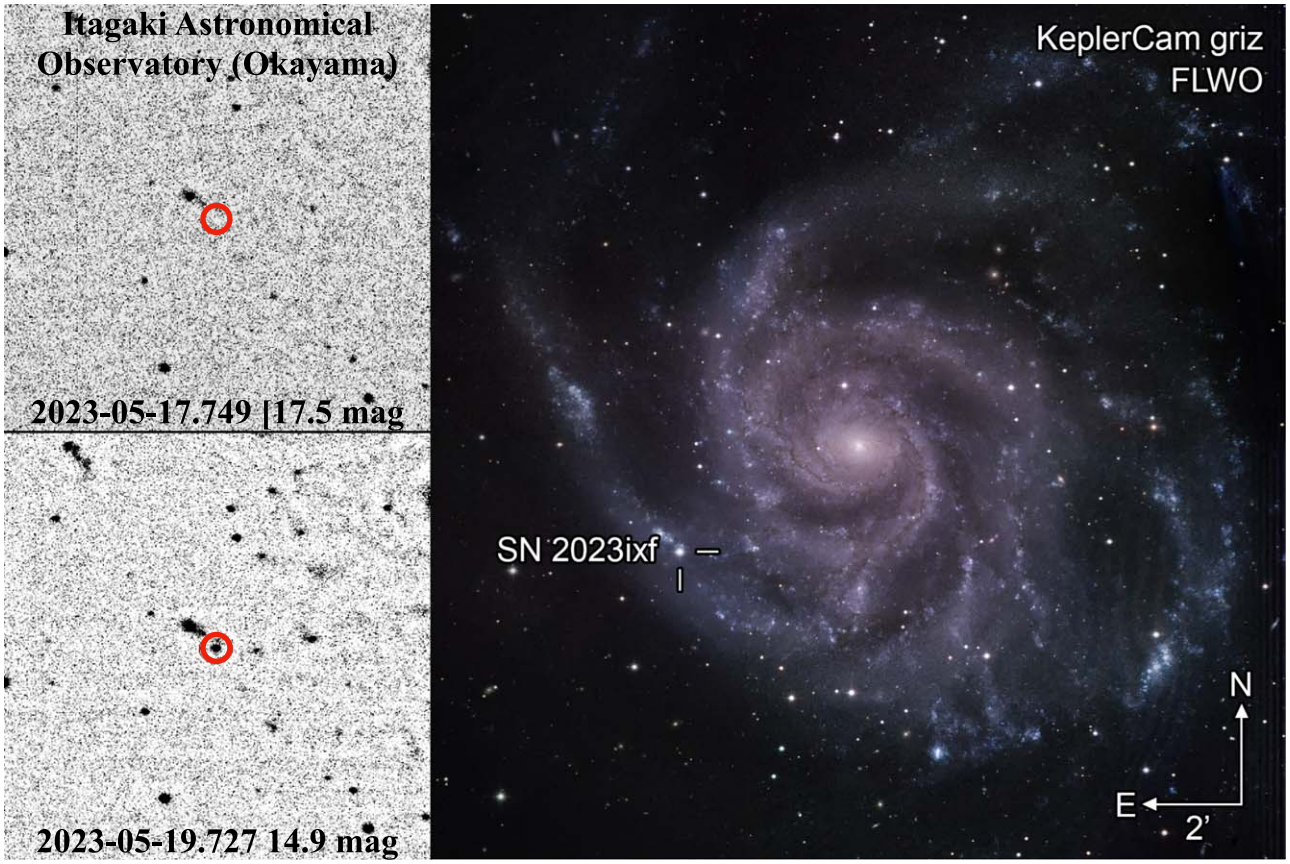

Figure 1. Left: last nondetection (top) and discovery (bottom) images taken by the Itagaki Astronomical Observatory. The red circle marks the position of SN 2023ixf. Right: color-composite (*griz*-band) image of SN 2023ixf and its host galaxy M101 taken by the Fred Lawrence Whipple Observatory. SN 2023ixf is located on a spiral arm with a nearby H II region roughly at solar metallicity and young (10^6–10^7 yr) stellar population (Hu et al. 2018).

(RSGs) from direct progenitor identifications (e.g., Van Dyk 2017), evidence is mounting that they experience elevated mass loss in the final months to decades before explosion, which is not predicted from standard stellar evolution theory. The presence of circumstellar material (CSM) from such mass loss can be inferred from early light-curve excess above shock-cooling emission (e.g., Morozova et al. 2018; Moriya et al. 2018; Förster et al. 2018; Hiramatsu et al. 2021), narrow high-ionization emission lines, so-called flash features excited by the radiation from shock breakout or the SN−CSM shock interface (e.g., Gal-Yam et al. 2014; Yaron et al. 2017; Dessart et al. 2017; Boian & Groh 2019, 2020; Terreran et al. 2022; Jacobson-Galán et al. 2022), and/or bremsstrahlung X-ray and synchrotron radio/millimeter emission from SN−CSM shock interaction (e.g., Chevalier 2017).

The recent discovery of Type II SN 2023ixf in M101 (Section 2) has allowed intensive multiwavelength observations. A dust-obscured RSG progenitor candidate with a possible periodic variability (≈1000-day period over the past ≈13 yr) has been identified in pre-explosion Hubble Space Telescope, Spitzer Space Telescope, and ground-based optical to infrared images (Pledger & Shara 2023; Kilpatrick et al. 2023; Jencson et al. 2023; Neustadt et al. 2023; Soraisam et al. 2023). Post-explosion observations have revealed early light-curve excess in the optical bands (Jacobson-Galan et al. 2023; Hosseinzadeh et al. 2023; Singh Teja et al. 2023; Sgro et al. 2023), flash features in low-to-high-resolution optical spectra (Yamanaka et al. 2023; Jacobson-Galan et al. 2023; Smith et al. 2023; Bostroem et al. 2023; Singh Teja et al. 2023), polarization measurements in spectropolarimetry (Vasylyev et al. 2023), early X-ray detections (Grefenstette et al. 2023), and millimeter nondetections (Berger et al. 2023).

Here we report our discovery of SN 2023ixf in Section 2 and follow-up photometric and spectroscopic observations, respectively, in the first month and week of its evolution in Section 3. In Section 4, we analyze the light curves and spectra. We then construct numerical light-curve models based on both continuous and eruptive mass-loss scenarios to extract the CSM formation history shortly before explosion in Section 5. Using this information, we discuss a consistent picture among the available observational constraints. Finally, we summarize our findings in Section 6.

2. Discovery and Classification

We (Itagaki 2023) discovered SN 2023ixf in M101 (Figure 1) on 2023 May 19.727 (UT dates are used throughout; MJD = 60083.727) at an unfiltered magnitude of 14.9 ± 0.1 at R.A. = $14^{h}03^{m}38^{s}.580$ and decl.=+54°18′42.″10 with the Itagaki Astronomical Observatory 0.35 m telescope (Okayama, Japan) + KAF-1001E CCD. The last nondetection was obtained with the same setup at 17.5 mag on 2023 May 17.749 (MJD = 60081.749). Subsequently, several other observers have reported limits and detections in the time window between our last nondetection and discovery (Perley & Irani 2023; Filippenko et al. 2023; Fulton et al. 2023; Mao et al. 2023; Koltenbah 2023; Chufarin et al. 2023). By taking the midpoint of the ≳20.4 mag limit on 2023 May 18.660

(MJD = 60082.660) from Mao et al. (2023) and the detection with 18.76 ± 0.25 mag on 2023 May 18.826 (MJD = 60082.826) from Chufarin et al. (2023), we estimate the epoch of SN first light (i.e., the moment when the SN light emerges from the stellar/CSM surface)[24] to be MJD = 60082.743 ± 0.083, corresponding to 0.98 days before our discovery.

Perley et al. (2023) obtained an optical spectrum of SN 2023ixf on 2023 May 19.93 (MJD = 60083.93; 4.9 hr after discovery) with the SPectrograph for the Rapid Acquisition of Transients (SPRAT; Piascik et al. 2014) on the Liverpool Telescope (LT; Steele et al. 2004), classifying it as an SN II with flash ionization features. Subsequent spectra have been obtained and reported by Teja et al. (2023) with the Himalaya Faint Object Spectrograph (HFOSC) on the 2 m Himalayan Chandra Telescope (HCT),[25] Stritzinger et al. (2023) with the Alhambra Faint Object Spectrograph and Camera (ALFOSC) on the Nordic Optical Telescope (NOT), Zhang et al. (2023) with the Beijing Faint Object Spectrograph and Camera (BFOSC) on the Xinglong 2.16 m Telescope (Fan et al. 2016), and Yaron (2023) with the Spectral Energy Distribution Machine (SEDM; Blagorodnova et al. 2018) on the Palomar 60-inch telescope, confirming the SN II classification.

In this work, we adopt a redshift of $z = 0.000804 \pm 0.000007$ (de Vaucouleurs et al. 1991)[26] and luminosity distance of $d_L = 6.9 \pm 0.1$ Mpc (distance modulus of $\mu = 29.194 \pm 0.039$ mag; Riess et al. 2022) to M101. We use the estimated first light (MJD = 60082.743 ± 0.083) as the zero-point reference for all phases unless otherwise specified.

3. Observations and Data Reduction

3.1. Photometry

Following the discovery, we continued monitoring SN 2023ixf with the Itagaki Astronomical Observatory 0.35, 0.5, and 0.6 m telescopes (Kochi, Okayama, and Yamagata, Japan) + unfiltered KAF-1001E CCD. Using our custom software, the aperture photometry was extracted and calibrated to Vega magnitudes from the Fourth US Naval Observatory CCD Astrograph Catalog (Zacharias et al. 2013). Additionally, we include the prediscovery amateur points listed in Section 2 in the subsequent analysis.

Through the Global Supernova Project (Howell & Global Supernova Project 2017), we obtained Las Cumbres Observatory (LCO; Brown et al. 2013) *UBVgriz*-band imaging with the SBIG and Sinistro cameras on the network of 0.4 and 1.0 m telescopes at the Haleakal ā Observatory (Hawaii, USA), McDonald Observatory (Texas, USA), and Teide Observatory (Canary Islands, Spain) starting on 2023 May 19.97 (MJD = 60083.97; 5.8 hr after discovery). The initial photometry up to 2023 May 30 (MJD = 60094) has been presented in Hosseinzadeh et al. (2023), and we extend it to 2023 June 18 (MJD = 60113; 30 days after discovery) following the same reduction procedures; *UBV* and *griz* point-spread function (PSF) photometry was calibrated to Vega (Landolt 1983, 1992) and AB (SDSS Collaboration et al. 2017) magnitudes, respectively, using `lcogtsnpipe`[27] (Valenti et al. 2016).

In addition, we triggered the Neil Gehrels Swift Observatory Ultraviolet/Optical Telescope (UVOT) follow-up imaging starting on 2023 May 20.27 (MJD = 60084.27; 13 hr after discovery). The aperture photometry was conducted and calibrated to Vega magnitudes using the pipeline for the Swift Optical Ultraviolet Supernova Archive (SOUSA; Brown et al. 2014), including the zero-points from Breeveld et al. (2011) and the sensitivity correction from 2020 September. The initial photometry up to 2023 May 21 (MJD = 60085) has been presented in Hosseinzadeh et al. (2023), and we extend it to 2023 June 9 (MJD = 60104). Unfortunately, the majority of the early Swift UVOT observations were saturated, and we only include the unsaturated observations analyzed by the standard SOUSA procedures.

Through our FLEET program (Gomez et al. 2020, 2023), we also obtained *griz*-band imaging with KeplerCam (Szentgyorgyi et al. 2005) on the 1.2 m Telescope at the Fred Lawrence Whipple Observatory (FLWO; Arizona, USA) starting on 2023 May 21.32 (MJD = 60085.32; 1.59 days after discovery). The PSF photometry was extracted and calibrated to AB magnitudes from the Pan-STARRS1 (Chambers et al. 2016) Data Release 2 (Flewelling et al. 2020).

To explore possible pre-explosion variability of SN 2023ixf, we also processed and examined the Zwicky Transient Facility (ZTF; Bellm et al. 2019; Graham et al. 2019), Asteroid Terrestrial-impact Last Alert System (ATLAS; Tonry et al. 2018; Smith et al. 2020), and Wide-field Infrared Survey Explorer (WISE; Wright et al. 2010; Mainzer et al. 2014) survey data. ZTF and ATLAS photometry were retrieved, respectively, from the ZTF forced-photometry service[28] (Masci et al. 2019, 2023) in the *g*, *r*, and *i* bands (from 2018 March 21; MJD = 58198) and the ATLAS Forced Photometry Server[29] (Shingles et al. 2021) in the *c* and *o* bands (from 2015 December 30; MJD = 57386). Then, we stacked them with a time window of every 10 days ($\lesssim$1% of the observed progenitor period; Kilpatrick et al. 2023; Jencson et al. 2023; Soraisam et al. 2023) for each filter to obtain deeper measurements.

For the ongoing NEOWISE all-sky survey in the W1 (3.4 μm) and W2 (4.5 μm) bands, we retrieved time-resolved coadded images of the field created as part of the unWISE project (Lang 2014; Meisner et al. 2018; UnWISE Team 2021). With the custom code (De et al. 2020) based on the ZOGY algorithm (Zackay et al. 2016), we performed image subtraction on the NEOWISE images using the full-depth coadds of the WISE and NEOWISE mission (obtained during 2010–2014) as reference images. Photometric measurements were obtained by performing forced PSF photometry at the transient position on the subtracted WISE images until the epoch of the unWISE data release (data acquired until 2022 May).

3.2. Spectroscopy

Through our FLEET program, we obtained optical spectra of SN 2023ixf with the FAST spectrograph (Fabricant et al. 1998; Tokarz & Roll 1997) on the FLWO 1.5 m Telescope starting on 2023 May 21.33 (MJD = 60085.33; 1.60 days after discovery). The combination of the 300 grating with a 3″-wide slit was used for dispersion, resulting in a wavelength coverage of

[24] This estimate is somewhat limited by the instrument sensitivity since the magnitude limit of 20.4 corresponds to a luminosity limit of $\sim 2 \times 10^{39}$ erg s^{-1}, roughly five times the estimated progenitor luminosity (Neustadt et al. 2023). We assume that the SN light reached the luminosity limit from the progenitor luminosity within the error in the epoch of SN first light (≈2 hr).

[25] http://www.iiap.res.in/iao/hfosc.html

[26] Via the NASA/IPAC Extragalactic Database: http://ned.ipac.caltech.edu/

[27] https://github.com/LCOGT/lcogtsnpipe

[28] https://ztfweb.ipac.caltech.edu/cgi-bin/requestForcedPhotometry.cgi

[29] https://fallingstar-data.com/forcedphot/

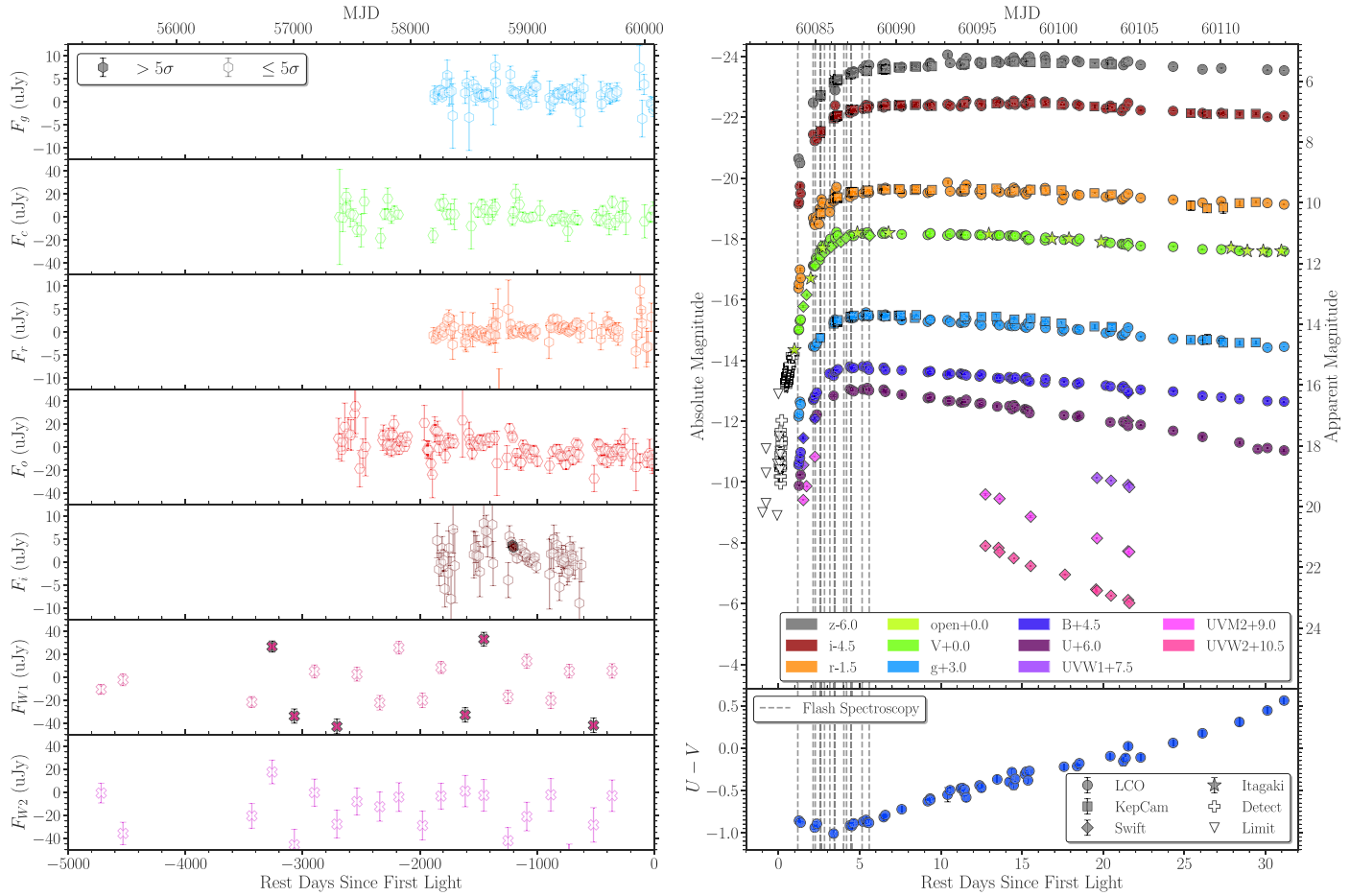

Figure 2. Left: pre-explosion differential flux measurements at the SN 2023ixf position in the ZTF *g,r,i* bands; ATLAS *c,o* bands; and WISE W1,W2 bands. Error bars denote 1σ uncertainties, and filled and open symbols are used for detections and 5σ limits, respectively. No significant variability ($>5\sigma$) is seen in the ZTF and ATLAS bands, except the two possible ZTF *i*-band detections. The few sporadic WISE W1 detections are due to imperfect subtraction of the nearby H II region (Figure 1). Right: multiband light curve (top) and $U-V$ color evolution (bottom) of SN 2023ixf. Amateur detections and limits are shown as the open plus signs and downward-pointing triangles, respectively, with no vertical offset. The gray vertical dashed lines mark the epochs of flash spectroscopy (Figure 3). SN 2023ixf is characterized by a rapid rise to the peak with blueward color evolution and a following bright plateau with redward color evolution. (The data used to create this figure will be available upon publication.)

(The data used to create this figure are available.)

4000 Å with a resolution $R \approx 1000$. One-dimensional spectra were extracted, reduced, and calibrated following standard procedures using PyRAF and flux-calibrated to a standard taken during the same night. Additionally, we retrieved the public LT/SPRAT, HCT/HFOSC, NOT/ALFOSC, Xinglong/BFOSC, and P60/SEDM spectra (listed in Section 2) via the Transient Name Server (TNS)[30] and include them in the subsequent analysis.

We also obtained high-resolution optical spectra on 2023 May 25 and 26 (MJD = 60089 and 60090; 5.6 and 6.5 days after discovery) with the Tillinghast Reflector Echelle Spectrograph (TRES; Szentgyorgyi & Furész 2007) on the FLWO 1.5 m Telescope (3850–9100 Å coverage with $R \approx$ 44,000) and on 2023 May 27, 28, and 29 (MJD = 60091, 60092, and 60093; 7.4, 8.4, and 9.4 days after discovery, respectively) with Hectoechelle (Szentgyorgyi et al. 1998) on the 6.5 m MMT Observatory (6460–6660 Å coverage centered on Hα with $R \approx 34{,}000$). The reduced data products were provided by the Smithsonian Astrophysical Observatory Optical/Infrared Telescope Data Center (Mink et al. 2005, 2007; Buchhave et al. 2010; Mink 2011). Given the lack of narrow flash features in the TRES and Hectoechelle spectra,[31] we only used them to measure the equivalent widths (EWs) of Na I D lines at the M101 redshift, yielding EW(D1) = 0.121 Å and EW(D2) = 0.180 Å. Using the Poznanski et al. (2012) calibration, these EWs translate to an M101 extinction of $E(B-V) = 0.032$ mag, in agreement with Lundquist et al. (2023) and Smith et al. (2023).

4. Analysis

All photometry and spectroscopy of SN 2023ixf are presented in Figures 2 and 3, respectively. We correct the photometry and spectroscopy for the Milky Way (MW) extinction of $E(B-V) = 0.0089$ mag (Schlafly & Finkbeiner 2011),[32] as well as the M101 extinction of $E(B-V) = 0.032$ mag (measured in

[30] https://www.wis-tns.org/

[31] This is due to the combination of a low signal-to-noise ratio (the first TRES spectrum) and a late phase coverage (the later TRES and Hectoechelle spectra).

[32] Via the NASA/IPAC Infrared Science Archive: https://irsa.ipac.caltech.edu/applications/DUST/

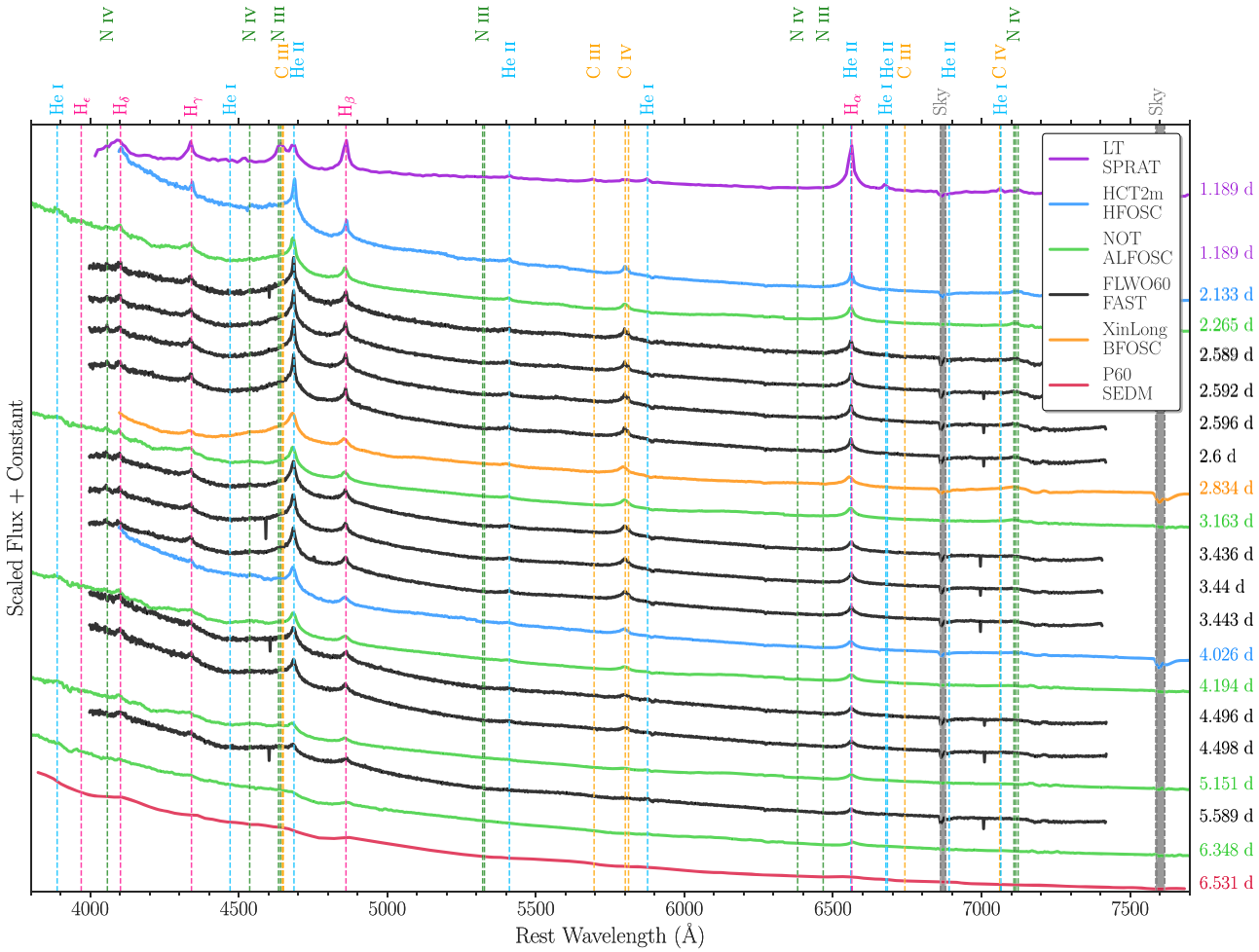

Figure 3. Spectral time series of SN 2023ixf. The phase of each spectrum with respect to first light is noted on the right side. The prominent flash features of H, He I, He II, C III, C IV, N III, and N IV persist up to 5.6 days, after which a blue featureless continuum dominates the spectra. A transition to a higher ionization state (i.e., C III → C IV) happens during the first two spectra, in line with the blueward $U - V$ color evolution (Figure 2). (The data used to create this figure will be available upon publication.)

(The data used to create this figure are available.)

Section 3), assuming the Fitzpatrick (1999) reddening law with $R_V = 3.1$ and extended to the WISE bands with the relative optical to infrared extinction values from Wang & Chen (2019).

4.1. Light-curve Evolution

We determine the detection significance (σ) of the ZTF, ATLAS, and WISE forced photometry from the ratio of measured flux (f) to its uncertainty ($f_{\rm err}$), i.e., $\sigma = |f|/f_{\rm err}$, where the absolute value of f is taken to account for both positive and negative variability. As shown in Figure 2, no significant pre-explosion variability ($\sigma > 5$) is seen at the SN 2023ixf position in ZTF ($m_{g,r,i} \gtrsim 21.8$, 22.0, 21.3) and ATLAS ($m_{c,o} \gtrsim 20.2$, 20.3) within ≈2700 days before first light (except the two possible ZTF i-band detections at 22.5 ± 0.2 mag ($\sigma = 6.1$) and 22.6 ± 0.2 mag ($\sigma = 5.3$) from ≈1205 to 1195 days before first light, which may allow short-term variability). This is consistent with the lack of long-term pre-explosion variability reported by Neustadt et al. (2023) in the deep Large Binocular Telescope (LBT) *UBVR*-band observations ($m \gtrsim 25$–26) from ≈5600 to 400 days before first light and extends such a coverage to 0.32 days before first light, albeit with the shallower limits. The few sporadic (nonperiodic) detections in the WISE W1 band ($\sim \pm 25$ μJy) are much higher than the variability ($\sim \pm 8$ μJy) seen in the Spitzer/IRAC Channel 1 (3.6 μm) observations with a similar temporal coverage (∼11.3 − 3.6 yr before explosion; Kilpatrick et al. 2023; Jencson et al. 2023; Soraisam et al. 2023), and visual inspections of the WISE difference images indicate imperfect image subtraction of the nearby H II region (Figure 1) due to its relatively large PSF size (FWHM ∼ 6″). Thus, we do not consider these as significant detections.

The light curve of SN 2023ixf is characterized by a rapid rise to a bright peak, from $M_V \approx -10$ to -18.2 mag within ≈5 days of first light (Figure 2), with a possible deviation from a single power-law rise in the first ≈1 day as noted by Hosseinzadeh et al. (2023). During this rising phase, the $U - V$ color shows blueward evolution[33] from -0.86 ± 0.03 mag (1.26 days) to -1.01 ± 0.04 mag (3.39 days). Assuming a blackbody spectral energy distribution (SED), this color evolution corresponds to a

[33] Similar blueward color evolution is also seen in the other bands (e.g., $g - r$), indicating a change in the continuum rather than in specific lines.

temperature rise from ≈12,000 to 16,000 K. Such color/temperature evolution is not expected from pure shock cooling and instead suggests a possible delayed shock breakout through dense CSM, in which a photosphere initially forms inside the unshocked optically thick CSM (e.g., Moriya et al. 2018; Förster et al. 2018; Haynie & Piro 2021; Khatami & Kasen 2023), as similarly seen in SN II 2018zd (Hiramatsu et al. 2021).

Following the bright peak, the light curve of SN 2023ixf settles on a plateau ($M_V \approx -17.6$ mag) extending to 30 days with a smooth decline rate of ≈0.03 mag day^{-1} from the peak (Figure 2). This plateau is on the bright and fast-declining ends of the SN II population (e.g., Anderson et al. 2014; Valenti et al. 2016; see also Jacobson-Galan et al. 2023; Singh Teja et al. 2023; Sgro et al. 2023). Coinciding with the peak, the $U-V$ color shows a transition to redward evolution, reaching ≈0.5 mag (≈6000 K) at 30 days. In contrast to the early blueward evolution, this redward evolution is typical of the SN II population (e.g., Valenti et al. 2016), likely suggesting a switch in the location of the photosphere to the SN ejecta as it overruns the dense CSM. If we assume a typical SN shock velocity of ∼10,000–15,000 km s^{-1} (e.g., Chevalier & Fransson 1994; Matzner & McKee 1999), the $U-V$ color transition at 3.4–4.4 days corresponds to a CSM radial extent of $\sim(3\text{–}6)\times10^{14}$ cm.

To extract CSM properties from the light-curve modeling in Section 5, we construct a pseudobolometric light curve of SN 2023ixf by fitting a blackbody SED to every epoch of photometry containing at least three filters obtained within 30 minutes of each other and then integrating the fitted blackbody SED over the optical coverage (*UBVRI*: 3250–8900 Å). For the unfiltered Itagaki photometry with a similar wavelength coverage (≈3200–9900 Å), we estimate its pseudobolometric correction at each epoch by linearly extrapolating or interpolating the blackbody temperatures from the multiband fits and taking the ratio of the integrated blackbody to observed flux convolved with the CCD response function. For the prediscovery amateur points, we crudely estimate their pseudobolometric luminosity assuming the same correction as the Itagaki discovery point, albeit with uncharacterized CCD/filter response functions. We note that the observed SED peaks are bluer than the U band in the first ≈10 days ($\gtrsim$10,000 K), and without reliable Swift UVOT coverage (Section 3.1) during this phase, the fitted blackbody temperatures may be underestimated by up to ∼10,000 K (e.g., Valenti et al. 2016; Arcavi 2022), which translates to a factor of ∼2 in the pseudobolometric luminosity.

4.2. Spectral Evolution

As shown in Figure 3, the early spectral evolution of SN 2023ixf is characterized by the flash features of H, He I, He II, C III, C IV, N III, and N IV on top of a blue continuum (see also Yamanaka et al. 2023; Jacobson-Galan et al. 2023; Smith et al. 2023; Bostroem et al. 2023; Singh Teja et al. 2023; Vasylyev et al. 2023). The N III $\lambda\lambda$4634, 4641 and C III $\lambda\lambda$4647, 4650 complex is comparable in line strength to He II λ4686 in the first spectrum at 1.19 days but then quickly fades in the second spectrum at 2.13 days. Similarly, C III λ5696 is comparable to C IV $\lambda\lambda$5801, 5812 at 1.19 days but fades at 2.13 days. This transition to a higher ionization state (C III → C IV) likely indicates a rise in temperature if we assume a smooth CSM density profile with constant elemental abundance (Boian & Groh 2019, 2020), as similarly seen in SN 2018zd (Hiramatsu et al. 2021). This is consistent with the possible delayed shock breakout seen in the $U-V$ color evolution (Figure 2).

The prominent flash features of He II λ4686 and C IV $\lambda\lambda$5801, 5812 persist until ≈5.6 and 4.5 days, respectively (Figure 3). Using these timescales as an alternate proxy to the color evolution[34] for the SN ejecta overrunning the dense CSM and assuming the same SN shock velocity as in Section 4.1, a radial CSM extent can be estimated as $\sim(4\text{–}7)\times10^{14}$ cm. Together with the $U-V$ color evolution, the flash spectral series indicates a confined CSM, broadly in agreement with the estimates from Jacobson-Galan et al. (2023), Smith et al. (2023), Bostroem et al. (2023), and Singh Teja et al. (2023).

5. Light-curve Modeling with CSM Interaction

Motivated by the early light curve (Section 4.1) and spectral evolution (Section 4.2), we consider two different mass-loss scenarios for producing the confined CSM: continuous and eruptive.

5.1. Continuous Mass Loss

As a first scenario, we explore "superwind" mass loss (e.g., Moriya et al. 2018; Förster et al. 2018) in which the continuous mass-loss rate is enhanced in the final years to decades before explosion by a few orders of magnitude ($\gtrsim10^{-3}\,M_\odot$ yr^{-1}) compared to a typical RSG mass-loss rate ($\sim10^{-5}\,M_\odot$ yr^{-1}; e.g., Goldman et al. 2017; Beasor et al. 2020). We assume a constant wind velocity of $v_{\rm wind} = 115$ km s^{-1} inferred by Smith et al. (2023) from the narrow Hα line profile in a high-resolution spectrum taken at 2.62 days. As noted by Smith et al. (2023), this velocity is higher than a typical RSG wind velocity of ∼20 km s^{-1} and likely requires radiative acceleration (Moriya et al. 2018; Tsuna et al. 2023) or eruptive mass loss (Section 5.2). With the estimated CSM radial extent of $\sim(3\text{–}7)\times10^{14}$ cm from the $U-V$ color and flash spectral evolution (Section 4), the velocity gives a mass-loss duration of ∼0.8–1.9 yr before explosion, which we explore here.

A broad range of possible masses, 8–20 $M_\odot$, has been reported for the progenitor of SN 2023ixf from pre-explosion imaging (Pledger & Shara 2023; Kilpatrick et al. 2023; Jencson et al. 2023; Soraisam et al. 2023). As a base model, we use an RSG model with a low mass ($M_{\rm ZAMS} = 12\,M_\odot$ and $M_{\rm final} = 11\,M_\odot$) and large radius ($907\,R_\odot$) from Goldberg & Bildsten (2020) given the observed bright light-curve plateau (Section 4.1). We note that according to the scaling relations for SN II light-curve plateaus (e.g., Popov 1993; Kasen & Woosley 2009; Sukhbold et al. 2016; Goldberg et al. 2019), these progenitor properties are degenerate with the explosion energy, which we vary to account for the uncertainties in the progenitor properties. A better characterization of the progenitor properties from light-curve modeling should be explored when the light curve is sampled to the radioactive tail. We also note that CSM estimates are less sensitive to a particular choice of degenerate parameters that result in a comparable CSM-free light curve (e.g., Goldberg & Bildsten 2020; Hiramatsu et al. 2021; Khatami & Kasen 2023).

[34] These two estimates do not agree perfectly, likely due to the difference in the optical depths they probe (i.e., optically thick photosphere and optically thin line emission; e.g., Morozova et al. 2020).

We use a combination of MESA (Paxton et al. 2011, 2013, 2015, 2018, 2019) and STELLA (Blinnikov et al. 1998, 2000; Blinnikov & Sorokina 2004; Baklanov et al. 2005; Blinnikov et al. 2006) for SN explosion and light-curve calculations, respectively. For the MESA explosion models, we vary the explosion energy ($E_{\rm exp} = (1.0–2.0) \times 10^{51}$ erg with 0.2×10^{51} erg increments), with a single value for the synthesized ^{56}Ni mass ($M_{\rm Ni} = 0.1\,M_\odot$), as it has no significant effect on the early light-curve evolution (e.g., Kasen & Woosley 2009; Goldberg et al. 2019; Kozyreva et al. 2019; Hiramatsu et al. 2021). We then use the output of these explosion models as an input to STELLA by adding a wind density profile, $\rho_{\rm wind}(r) = \dot{M}_{\rm wind}/4\pi r^2 v_{\rm wind}$, with varying mass-loss rates ($\dot{M}_{\rm wind} = 10^{-4} - 1\,M_\odot$ yr^{-1} with 0.5 dex increments) and durations ($t_{\rm wind} = 0.5$–2.0 yr with 0.5 yr increments); the CSM mass is given by $M_{\rm CSM} = \dot{M}_{\rm wind} t_{\rm wind}$. We use 700 and 100 spatial zones for the SN ejecta and CSM, respectively, and 100 frequency bins. A more detailed description of the MESA+STELLA workflow can be found in previous works (e.g., Paxton et al. 2018; Goldberg et al. 2019; Hiramatsu et al. 2021).

In Figure 4, the pseudobolometric light curves of both CSM-free models and a subset of CSM models are compared with that of SN 2023ixf. In these model comparisons, we reference the phase with respect to the Itagaki discovery (the first point with the known CCD characteristic; Section 4.1) and shift the model phase to match the discovery point since the "first light" is not well defined in the models. The CSM-free models fail to reproduce the first ≈20 days of light-curve evolution (Figure 4, top left), which highlights the need for CSM interaction.

In the following CSM model comparison, we choose an explosion energy of $E_{\rm exp} = 1.0 \times 10^{51}$ erg, as its CSM-free model provides the best fit at 30 days after discovery when the effect of CSM interaction is expected to become less significant (but we do not intend to constrain $E_{\rm exp}$ given its degeneracy with the progenitor properties). For a given mass-loss rate of $\dot{M}_{\rm wind} = 1.0\,M_\odot$ yr^{-1}, the peak luminosity is reasonably well reproduced by a mass-loss duration of $t_{\rm wind} = 1.0$ yr (Figure 4, top right). A longer (shorter) $t_{\rm wind}$ results in a peak that is too wide (narrow). For $\dot{M}_{\rm wind} = 0.3\,M_\odot$ yr^{-1}, $t_{\rm wind} = 2.0$ yr better reproduces the peak luminosity. With a higher explosion energy of $E_{\rm exp} = 2.0 \times 10^{51}$ erg, these mass-loss estimates are reduced by ≈0.5 dex (i.e., $\dot{M}_{\rm wind} \approx 0.1$–$0.3\,M_\odot$ yr^{-1} for $t_{\rm wind} = 2.0 - 1.0$ yr), albeit with an overshoot of the plateau luminosity at >20 days (as already seen in Figure 4, top left). Below $\dot{M}_{\rm wind} = 0.1\,M_\odot$ yr^{-1}, we do not find any models with a peak luminosity $\gtrsim 3 \times 10^{42}$ erg s^{-1} (even with $E_{\rm exp} = 2.0 \times 10^{51}$ erg) in this confined CSM configuration with $v_{\rm wind} = 115$ km s^{-1}. Thus, we estimate a range of mass-loss history to be $\dot{M}_{\rm wind} = 0.1$–$1.0\,M_\odot$ yr^{-1} for $t_{\rm wind} = 2.0 - 1.0$ yr to reproduce the peak luminosity.

For $t_{\rm wind} = 1.0$ and 2.0 yr, the effect of varying $\dot{M}_{\rm wind}$ is shown in Figure 4 (bottom left). As discussed, $\dot{M}_{\rm wind} \geqslant 0.3\,M_\odot$ yr^{-1} is required to fit the peak luminosity well, and $\dot{M}_{\rm wind} \lesssim 10^{-3}\,M_\odot$ yr^{-1} has negligible effects on the peak luminosity. However, one difficulty with $\dot{M}_{\rm wind} = 0.3$–$1.0\,M_\odot$ yr^{-1} for $t_{\rm wind} = 2.0 - 1.0$ yr is that it overproduces the luminosity in prediscovery phase. The zoomed-in version to this phase is shown in Figure 4 (bottom right). For $t_{\rm wind} = 1.0$ yr, $\dot{M}_{\rm wind} = 0.1\,M_\odot$ yr^{-1} captures the early excess (whose presence is first noted by Hosseinzadeh et al. 2023) down to ≈0.6 days before discovery and the following rise up to ≈1 day after discovery, albeit with an overshoot of the deep upper limit at $\approx 8 \times 10^{38}$ erg s^{-1} by ≈0.3 days. Therefore, we speculate a time-variable mass-loss rate in the final $2 - 1$ yr before explosion in which a lower mass-loss rate (≈ 0.01–$0.1\,M_\odot$ yr^{-1}) follows a higher one (≈ 0.1–$1\,M_\odot$ yr^{-1}) within the explosion properties explored here.[35] Assuming that the lower mass-loss rate is responsible for the first ∼2 days of light-curve evolution after first light as the SN–CSM shock layer propagates through, this transition might have happened at ∼0.7–0.4 yr before explosion (with an SN shock velocity of ∼10,000–15,000 km s^{-1}). Then, the total CSM mass could be estimated as ∼0.1–0.7 $M_\odot$.

5.2. Eruptive Mass Loss

Another scenario usually considered for a dense CSM is eruptive mass loss months to years before core collapse. Such outbursts are observed for a significant fraction of SNe IIn (strongly interacting SNe with narrow H emission lines throughout their evolution; Ofek et al. 2013, 2014; Margutti et al. 2014; Strotjohann et al. 2021; Hiramatsu et al. 2023). While such detections are limited for more standard SNe II (Kochanek et al. 2017; Johnson et al. 2018; but see Jacobson-Galán et al. 2022), this scenario is recently found to be favored over the superwind model from modeling of SN II progenitors (Davies et al. 2022).

For this scenario, we follow and extend the methods of Tsuna et al. (2023), which used the open-source code CHIPS (Takei et al. 2022) to simulate mass eruption, followed by SNEC (Morozova et al. 2015) for calculating the bolometric light curve. The mass loss is assumed to be triggered by energy injection at the base of the envelope, which forms a shock that propagates to the surface and expels a part of the envelope. The model is characterized by two parameters: the injected energy and the amount of time from injection to core collapse. These control the mass, velocity, and extent of the CSM at core collapse.

We extend the model grid from Tsuna et al. (2023) while using the same RSG progenitor as the earlier work evolved by MESA of $15\,M_\odot$ at ZAMS, which is within the mass range inferred for the SN 2023ixf progenitor. The progenitor has a mass of $12.8\,M_\odot$ and a radius of $670\,R_\odot$ at the time of energy injection, with modeling of mixing length and stellar wind outlined in Tsuna et al. (2023). This progenitor choice is different from that in Section 5.1; however, as noted, a variation in explosion energies should account for the difference given the light-curve scaling relations. For the injected energy, the CHIPS code uses the injected energy scaled to the binding energy of the envelope ($\approx 4.86 \times 10^{47}$ erg for this progenitor star), defined in the code as $f_{\rm inj}$. A fraction of the envelope is unbound for $f_{\rm inj} \gtrsim 0.2$, and we thus consider a range of values $f_{\rm inj} = [0.2, 0.25, 0.3, 0.4, 0.5, 0.6, 0.7]$.

We first simulate explosions with CSM models of 1 and 2 yr from energy injection, motivated by the deep LBT limits on apparent pre-SN outbursts of the progenitor up to about 400 days prior to the SN (Neustadt et al. 2023).[36] For the range of $f_{\rm inj}$, the dense CSM expands in these 2 yr to radii of $\approx (2$–$7) \times 10^{14}$ cm, with respective masses of ≈0.04–1.7 $M_\odot$.

[35] This may also be possible with an increasing $v_{\rm wind}$, as $\rho_{\rm wind} \propto \dot{M}_{\rm wind}/v_{\rm wind}$. But it would create wind-to-wind collision, which should be explored in future work.

[36] We note that it takes several months from energy injection for the shock to propagate to the surface and be seen as an outburst.

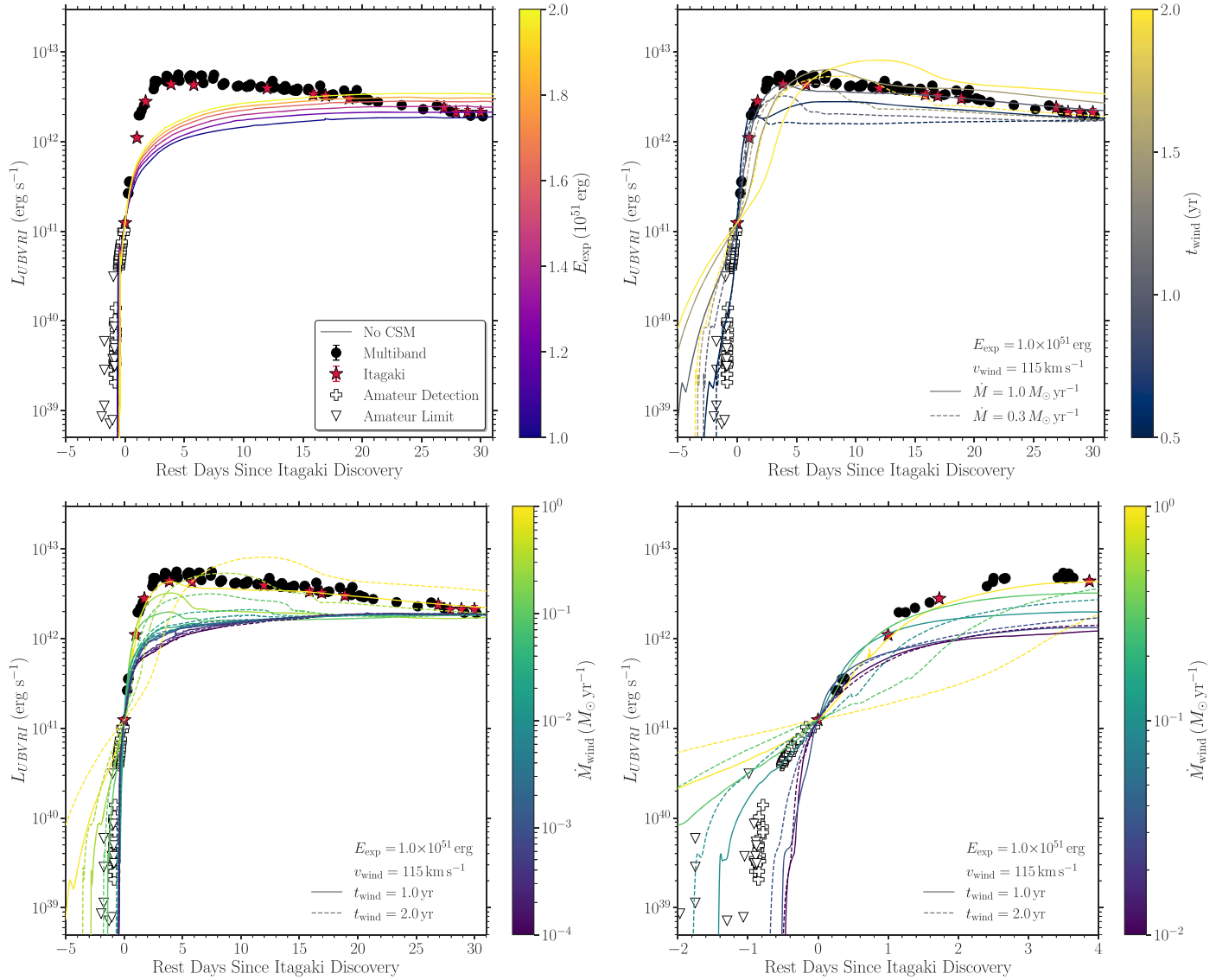

Figure 4. Comparison of the pseudobolometric light curve of SN 2023ixf with CSM-free light-curve models with varying explosion energies ($E_{\rm exp}$; top left), and continuous mass-loss light-curve models with a single $E_{\rm exp}$ (1.0×10^{51} erg) and CSM velocity ($v_{\rm wind} = 115$ km s^{-1}): two fixed mass-loss rates ($\dot{M}_{\rm wind}$) with varying mass-loss durations ($t_{\rm wind}$; top right), two fixed $t_{\rm wind}$ with varying $\dot{M}_{\rm wind}$ (bottom left), and a zoomed-in version to the early phase (bottom right). The phase is shifted with respect to the Itagaki discovery. CSM-free and minimal-CSM models are unable to reproduce the luminous peak/plateau up to 20 days, and the luminosity excess requires $\dot{M}_{\rm wind} = 0.3$–$1\ M_\odot$ yr^{-1} for $t_{\rm wind} = 2 - 1$ yr before explosion. The mismatch in the prediscovery excess may suggest a decreasing $\dot{M}_{\rm wind}$ toward the explosion.

As in Tsuna et al. (2023), we then attach the evolved envelope to the core of the MESA model and simulate the explosion using SNEC. We excise the inner $1.8\,M_\odot$ of the star and inject energy at the inner $0.1\,M_\odot$ as a thermal bomb. We consider the final explosion energy of $E_{\rm exp} = 10^{51}$ and 2×10^{51} erg.

Using the bolometric luminosity output by SNEC, we assume that the emission is thermalized at the photosphere and calculate the luminosities in the *UBVRI* bands (3250 – 8900 Å). The resulting light curves for injections 1 and 2 yr before the SN are shown as dashed and dotted lines in Figure 5, respectively; a reference model with no CSM is shown with a dashed–dotted line. As in Section 5.1, the model with no CSM has a monotonic rise and thus significantly underestimates around the peak. The bright plateau of SN 2023ixf after the peak is well reproduced by the cooling emission of the shocked CSM (e.g., Piro 2015; Piro et al. 2021), for a range of $f_{\rm inj} \approx 0.25$–0.4. While no perfect match to observations is found, the 1 yr model with $E_{\rm exp} = 10^{51}$ erg appears to best reproduce both the rise timescale and the plateau luminosity.[37] The masses of the CSM in these models are $M_{\rm CSM} \approx 0.3$–$1\,M_\odot$, which agrees with the masses estimated in Section 5.1.

A notable problem for the models is that they generally overpredict the luminosity around the peak. One possible reason for this is a departure from thermal equilibrium in the postshock region around breakout. In our CSM model, the density sharply drops around the breakout radius, which can also accelerate the shock. A low CSM density and, more importantly, a large shock velocity ($\gtrsim 10^4$ km s^{-1}) can both lead to deviation from thermal equilibrium

[37] For a fixed $f_{\rm inj}$, the CSM extent generally scales with the escape velocity of the RSG progenitor. Thus, the required timescale can change for different progenitor models, but this change is expected to be of order unity.

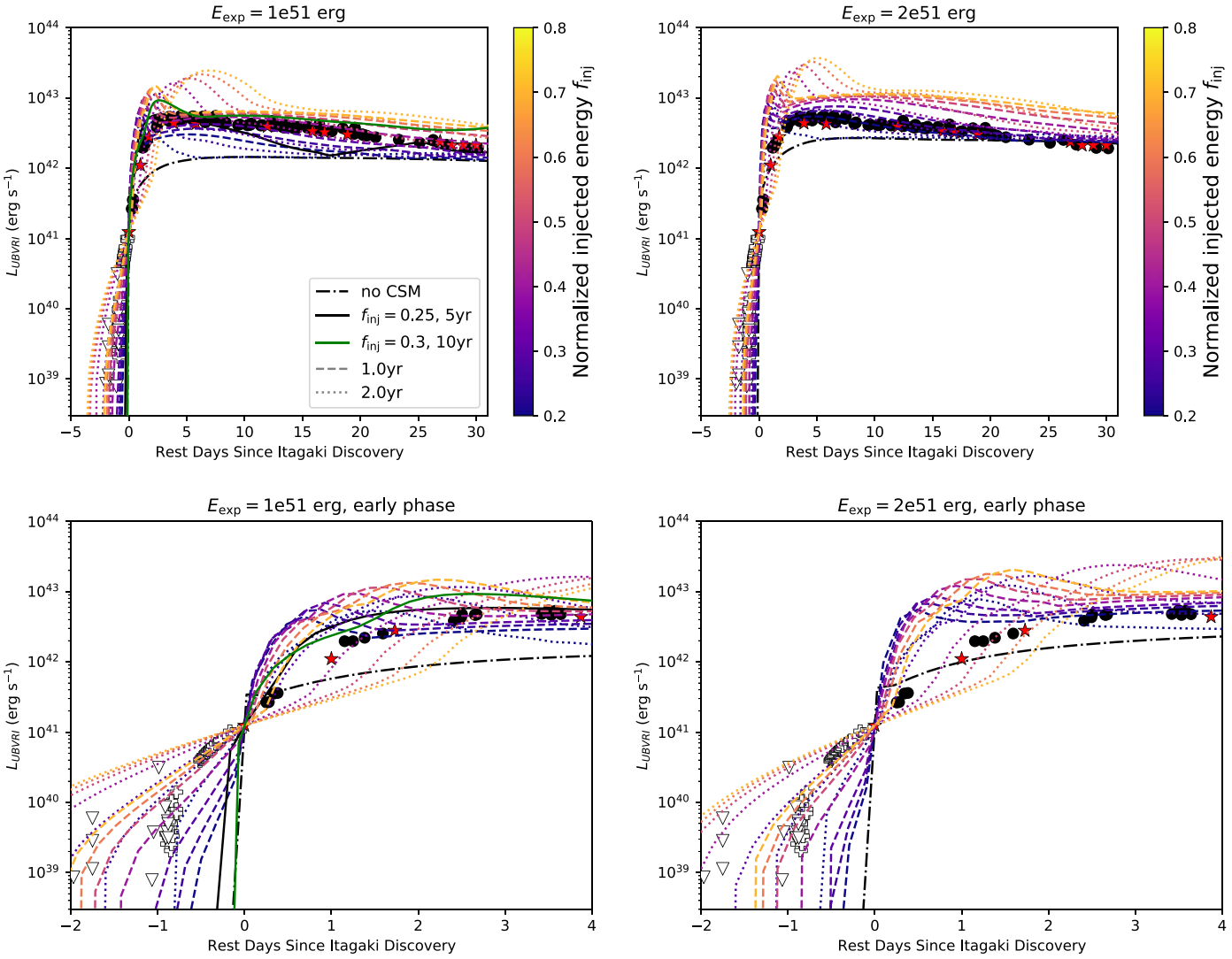

Figure 5. Optical light curves of interacting SNe for the eruptive mass-loss model, color-coded by the normalized injected energy, f_{inj}. The dashed and dotted lines are explosions with CSM formed by energy injections 1 and 2 yr before the SN, respectively. The black dashed–dotted lines show the case for the progenitor with no CSM. The green (black) solid lines in the left panels are models with an extended CSM expelled 10 (5) yr before the SN with $f_{inj} = 0.3$ (0.25). The data points from observations are the same as in Figure 4.

(Nakar & Sari 2010; Svirski et al. 2012; Haynie & Piro 2021), which reduces the optical luminosity.

Another possibility for the eruptive case is a much earlier mass ejection, where breakout from a less dense CSM powers the peak and continued interaction powers the plateau. We explored models with longer intervals between the eruption and SN and found that two models, with energy injection 10 (5) yr before the SN with $f_{inj} = 0.3$ (0.25), reproduce the light curves better around the peak than the 1–2 yr models for $E_{exp} = 10^{51}$ erg. These light curves are shown with solid lines in Figure 5. In these models, the CSM extends to $\approx 10^{15}$ (5×10^{14}) cm with mass of ≈ 0.06 (0.04) $M_{\odot}$, which is consistent with the results of Jacobson-Galan et al. (2023). However, as we explain in the next section, this model of early eruption is less preferred, as it may face two challenges: the nearly periodic pre-explosion variability (Kilpatrick et al. 2023; Jencson et al. 2023; Soraisam et al. 2023), and the early X-ray detection (Grefenstette et al. 2023).

5.3. Comparison to Other Observational Constraints

In both the continuous and eruptive mass-loss cases, we find that the dense CSM (0.1–1 $M_{\odot}$) confined within (3–7) $\times 10^{14}$ cm is able to reproduce the early light-curve evolution. Here we discuss other observational constraints obtained thus far and their implications for our mass-loss models.

The infrared light curve of the progenitor from 2012 is consistent with a nearly regular periodic variability, with no evidence of an additional precursor emission (Kilpatrick et al. 2023; Jencson et al. 2023; Soraisam et al. 2023). The absence of change in dust optical depth between 5600 and 400 days before explosion has independently constrained the potential outburst to be $\lesssim$3–5 times brighter than the progenitor's original luminosity of $\sim 10^5$ $L_{\odot} = 4 \times 10^{38}$ erg s^{-1} (Neustadt et al. 2023).

The continuous mass-loss scenario may result in precursor emission owing to the sustained energy injection that generates the outflow. With the inferred CSM properties, we estimate the

luminosity of a possible precursor to be $\lesssim 2 \times 10^{39}$ erg s^{-1} from Matsumoto & Metzger (2022) in a dust-free environment. This is within the allowed luminosity range without altering the dust optical depth too much ($\tau_V = 10$–13; Neustadt et al. 2023), and such an obscured precursor is consistent with the pre-explosion limits presented in Figure 2, as well as the deeper LBT limits (Neustadt et al. 2023) if the mass loss happens within ≈400 days before explosion (i.e., outside the LBT coverage). If the mass loss is instead driven by pulsation (e.g., Yoon & Cantiello 2010), a less luminous precursor is likely expected, which may provide a more natural explanation for the periodic progenitor variability.

For the eruptive mass-loss scenario, the precursor models of Tsuna et al. (2023) are dust-free and cannot be directly constrained from the pre-explosion observations of SN 2023ixf. However, the precursor emission for models with $f_{\rm inj} = 0.25$ and 0.3, which lasts for $\lesssim$1 yr from eruption, is only $\lesssim$1 mag brighter (Tsuna et al. 2023) and is thus within the allowed luminosity range to avoid significant change of the dust optical depth (Neustadt et al. 2023). A caveat is that for eruptions much earlier than 2 yr before the SN, this scenario does not explain the observed periodic variability after the eruption. An eruption perturbs and oscillates the leftover envelope, which may cause the variability, but there is no evident reason that both its timescale and amplitude would be similar to the observed one. It is worthwhile to study the precursor emission in dusty environments, as well as its later oscillation, to quantitatively constrain this scenario.

The X-ray data obtained 4 days after explosion suggest a rather tenuous CSM, with a mass-loss rate of $\approx 3 \times 10^{-4}\,M_\odot\,{\rm yr}^{-1}$ for an assumed CSM velocity of 50 km s^{-1} (Grefenstette et al. 2023). Since the radius of the CSM probed is $\gtrsim$(4–6) × 10^{14} cm for an SN shock velocity of ∼10,000–15,000 km s^{-1}, this does not contradict our preferred models (both continuous and eruptive) of the compact, dense CSM. However, this is in tension with an eruption 5–10 yr before explosion, whose density is higher than this by about an order of magnitude. An asymmetric CSM may alleviate this problem, if the line of sight is not subtended by the dense CSM inferred from the optical light curve. An asymmetric CSM is also suggested from early spectra (Smith et al. 2023; Vasylyev et al. 2023) and millimeter nondetections ($\lesssim$mJy at 230 GHz; Berger et al. 2023), although the latter require the line of sight to be in the dense part of the CSM assuming a single wind density profile. Alternatively, the millimeter nondetections may be explained with our confined CSM models in that the early nondetections ($\lesssim$4 days) are due to free–free absorption by the confined CSM, while the later nondetections are due to weaker synchrotron emission from the underlying extended CSM (∼10^{-4} to $10^{-5}\,M_\odot\,{\rm yr}^{-1}$). This merits further investigations, especially with a recent fainter radio detection (≈40 μJy at 10 GHz) at 29 days after first light (Matthews et al. 2023).

Estimates based on spectra (Jacobson-Galan et al. 2023; Bostroem et al. 2023) find a CSM of $M_{\rm CSM} \approx 10^{-2}$–$0.1\ M_\odot$, much smaller than our results of 0.1–1 $M_\odot$. This may be due to the light curve and spectra probing different parts of the CSM (see, e.g., Morozova et al. 2020, for a similar discussion on SN II 2013fs). Indeed, the light-curve model from Jacobson-Galan et al. (2023) with such a lower $M_{\rm CSM}$ underproduces the luminosity in the first week of its evolution (see also Singh Teja et al. 2023, for a similar discrepancy even with extremely large explosion energies of (2–5) × 10^{51} erg). Furthermore, the density profiles of our preferred CSM models are different from a wind profile assumed in spectral modeling. As in Section 5.1, a single wind profile has difficulties explaining both the light-curve rise and plateau. The CSM from mass eruption is also expected to have a profile much different from that of a wind (Kuriyama & Shigeyama 2020; Morozova et al. 2020; Tsuna et al. 2021; Tsang et al. 2022).

6. Summary

We have presented our discovery of SN 2023ixf in M101 at 6.9 Mpc and follow-up photometric and spectroscopic observations, respectively, in the first month and week of its evolution. Our observations have revealed the following:

1. A rapid rise (≈5 days) to a luminous light-curve peak ($M_V \approx -18.2$ mag) and plateau ($M_V \approx -17.6$ mag) extending to 30 days after first light with a fast decline rate of ≈0.03 mag day^{-1}.
2. Blueward $U-V$ color evolution in the first 4.4 days toward the light-curve peak followed by redward color evolution during the light-curve plateau.
3. Prominent flash spectral features of H, He I, He II, C III, C IV, N III, and N IV persisting up to 4.5–5.6 days after first light.
4. A transition to a higher spectral ionization state (i.e., C III → C IV) in the first 2.1 days after first light.

These observed properties are not expected from pure shock cooling emission and instead suggest a delayed shock breakout from a dense CSM confined within ∼(3–7) × 10^{14} cm. Motivated by this, we have constructed numerical light-curve models based on both continuous and eruptive mass-loss scenarios shortly before explosion. Our key findings are as follows:

1. For the continuous mass-loss scenario, we infer a range of mass-loss history with 0.1–1.0 $M_\odot$ yr^{-1} in the final 2.0–1.0 yr before explosion, with a potentially decreasing mass loss of 0.01–0.1 $M_\odot$ yr^{-1} toward the explosion ($\lesssim$0.7–0.4 yr) to reproduce the rapid rise and luminous peak.
2. For the eruptive mass-loss scenario, we favor energy injections of ∼10^{47} erg at the base of the envelope in the final year before explosion, which releases 0.3–1 $M_\odot$ of the envelope as CSM. The mass and extent of the CSM broadly agree with the continuous scenario.

These confined, dense CSM models are compatible with the early X-ray detections, millimeter nondetections, and possibly the progenitor variability without clear outbursts before the final ∼1 yr of explosion.

Given its proximity, SN 2023ixf will remain as a primarily SN target for multiwavelength follow-up observations in the coming years. In ultraviolet to infrared, a fully sampled light curve up to a radioactive tail will allow better characterizations of the progenitor and explosion properties. Nebular-phase spectra have potential to constrain the progenitor mass, possibly better than the current pre-explosion estimates. Deviations from a smooth light-curve plateau and/or tail, or continued X-ray and/or radio/millimeter emission, will provide unique opportunities to probe the mass-loss history in the final years to decades of its progenitor evolution.

Acknowledgments

We are grateful to Anthony Piro, Jim Fuller, Ken'ichi Nomoto, Takashi Moriya, and Charles Kilpatrick for useful discussions; to Warren Brown, Pascal Fortin, Murdock Hart, David Latham, and Jessica Mink for scheduling and reducing FLWO KeplerCam, FAST, and TRES observations; and to Nelson Caldwell, Daniel Fabricant, and Sean Moran for scheduling the MMT Hectochelle observations.

The Berger Time-Domain research group at Harvard is supported by the NSF and NASA. The LCO supernova group is supported by NSF grants AST-1911151 and AST-1911225. D.T. is supported by the Sherman Fairchild Postdoctoral Fellowship at the California Institute of Technology. The Flatiron Institute is supported by the Simons Foundation. This publication was made possible through the support of an LSSTC Catalyst Fellowship to K.A.B., funded through grant 62192 from the John Templeton Foundation to LSST Corporation. The opinions expressed in this publication are those of the authors and do not necessarily reflect the views of LSSTC or the John Templeton Foundation. I.A. acknowledges support from the European Research Council (ERC) under the European Union's Horizon 2020 research and innovation program (grant agreement No. 852097), from the Israel Science Foundation (grant No. 2752/19), from the United States—Israel Binational Science Foundation (BSF), and from the Israeli Council for Higher Education Alon Fellowship. J.C.W. and J.V. are supported by NSF grant AST1813825. J.V. is also supported by OTKA grant K-142534 of the National Research, Development and Innovation Office, Hungary.

This work makes use of observations from KeplerCam on the 1.2 m telescope and FAST and TRES on the 1.5 m telescope at the Fred Lawrence Whipple Observatory. Observations reported here were obtained at the MMT Observatory, a joint facility of the Smithsonian Institution and the University of Arizona. This paper uses data products produced by the OIR Telescope Data Center, supported by the Smithsonian Astrophysical Observatory.

This work makes use of observations from the Las Cumbres Observatory global telescope network. The authors wish to recognize and acknowledge the very significant cultural role and reverence that the summit of Haleakalā has always had within the indigenous Hawaiian community. We are most fortunate to have the opportunity to conduct observations from the mountain.

We thank the support of the staffs at the Neil Gehrels Swift Observatory.

This work has made use of data from the Zwicky Transient Facility (ZTF). ZTF is supported by NSF grant No. AST-1440341 and a collaboration including Caltech, IPAC, the Weizmann Institute for Science, the Oskar Klein Center at Stockholm University, the University of Maryland, the University of Washington, Deutsches Elektronen-Synchrotron and Humboldt University, Los Alamos National Laboratories, the TANGO Consortium of Taiwan, the University of Wisconsin–Milwaukee, and Lawrence Berkeley National Laboratories. Operations are conducted by COO, IPAC, and UW. The ZTF forced-photometry service was funded under the Heising-Simons Foundation grant No. 12540303 (PI: Graham).

This work has made use of data from the Asteroid Terrestrial-impact Last Alert System (ATLAS) project. ATLAS is primarily funded to search for near-Earth asteroids through NASA grant Nos. NN12AR55G, 80NSSC18K0284, and 80NSSC18K1575; by-products of the NEO search include images and catalogs from the survey area. This work was partially funded by Kepler/K2 grant No. J1944/80NSSC19K0112, HST grant No. GO-15889, and STFC grant Nos. ST/T000198/1 and ST/S006109/1. The ATLAS science products have been made possible through the contributions of the University of Hawaii Institute for Astronomy, the Queen's University Belfast, the Space Telescope Science Institute, the South African Astronomical Observatory, and the Millennium Institute of Astrophysics (MAS), Chile.

The PS1 and the PS1 public science archives have been made possible through contributions by the Institute for Astronomy, the University of Hawaii, the Pan-STARRS Project Office, the Max-Planck Society and its participating institutes, the Max Planck Institute for Astronomy, Heidelberg and the Max Planck Institute for Extraterrestrial Physics, Garching, Johns Hopkins University, Durham University, the University of Edinburgh, the Queen's University Belfast, the Harvard-Smithsonian Center for Astrophysics, the Las Cumbres Observatory Global Telescope Network Incorporated, the National Central University of Taiwan, the Space Telescope Science Institute, NASA under grant No. NNX08AR22G issued through the Planetary Science Division of the NASA Science Mission Directorate, NSF grant No. AST-1238877, the University of Maryland, Eotvos Lorand University, the Los Alamos National Laboratory, and the Gordon and Betty Moore Foundation.

This publication makes use of data products from the Wide-field Infrared Survey Explorer, which is a joint project of the University of California, Los Angeles, and the Jet Propulsion Laboratory/California Institute of Technology, funded by the National Aeronautics and Space Administration.

This research has made use of the NASA Astrophysics Data System (ADS), the NASA/IPAC Extragalactic Database (NED), and NASA/IPAC Infrared Science Archive (IRSA, which is funded by NASA and operated by the California Institute of Technology) and IRAF (which is distributed by the National Optical Astronomy Observatory, NOAO, operated by the Association of Universities for Research in Astronomy, AURA, Inc., under cooperative agreement with the NSF).

TNS is supported by funding from the Weizmann Institute of Science, as well as grants from the Israeli Institute for Advanced Studies and the European Union via ERC grant No. 725161.

Facilities: ADS, ATLAS, FLWO (FAST, KeplerCam, TRES), IRSA, LCO (SBIG, Sinistro), MMT (Hectoechelle), NED, PS1, Swift (UVOT), WISE, ZTF.

Software: Astropy (Astropy Collaboration et al. 2018), `atlas-fp` (https://gist.github.com/thespacedoctor/86777fa5a9567b7939e8d84fd8cf6a76), BANZAI (McCully et al. 2018), `CHIPS` (Takei et al. 2022), `emcee` (Foreman-Mackey et al. 2013), `lcogtsnpipe` (Valenti et al. 2016), Matplotlib (Hunter 2007), `MESA` (Paxton et al. 2011, 2013, 2015, 2018, 2019), NumPy (Oliphant 2006), `photutils` (Bradley et al. 2022), PyRAF (Science Software Branch at STScI 2012), SciPy (Virtanen et al. 2020), seaborn (Waskom et al. 2020), `SExtractor` (Bertin & Arnouts 1996), `STELLA` (Blinnikov et al. 1998, 2000,Blinnikov2004ApSS29013B,Baklanov et al. 2005; Blinnikov et al. 2006), `SNEC` (Morozova et al. 2015).

ORCID iDs

Daichi Hiramatsu https://orcid.org/0000-0002-1125-9187
Daichi Tsuna https://orcid.org/0000-0002-6347-3089
Edo Berger https://orcid.org/0000-0002-9392-9681

Jared A. Goldberg https://orcid.org/0000-0003-1012-3031
Sebastian Gomez https://orcid.org/0000-0001-6395-6702
Kishalay De https://orcid.org/0000-0002-8989-0542
Griffin Hosseinzadeh https://orcid.org/0000-0002-0832-2974
K. Azalee Bostroem https://orcid.org/0000-0002-4924-444X
Peter J. Brown https://orcid.org/0000-0001-6272-5507
Iair Arcavi https://orcid.org/0000-0001-7090-4898
Allyson Bieryla https://orcid.org/0000-0001-6637-5401
Peter K. Blanchard https://orcid.org/0000-0003-0526-2248
Gilbert A. Esquerdo https://orcid.org/0000-0002-9789-5474
Joseph Farah https://orcid.org/0000-0003-4914-5625
D. Andrew Howell https://orcid.org/0000-0003-4253-656X
Tatsuya Matsumoto https://orcid.org/0000-0002-9350-6793
Curtis McCully https://orcid.org/0000-0001-5807-7893
Megan Newsome https://orcid.org/0000-0001-9570-0584
Estefania Padilla Gonzalez https://orcid.org/0000-0003-0209-9246
Craig Pellegrino https://orcid.org/0000-0002-7472-1279
Jaehyon Rhee https://orcid.org/0000-0001-9214-7437
Giacomo Terreran https://orcid.org/0000-0003-0794-5982
József Vinkó https://orcid.org/0000-0001-8764-7832
J. Craig Wheeler https://orcid.org/0000-0003-1349-6538

References

Anderson, J. P., González-Gaitán, S., Hamuy, M., et al. 2014, ApJ, 786, 67
Arcavi, I. 2017, in Handbook of Supernovae, ed. A. W. Alsabti & P. Murdin (Berlin: Springer), 239
Arcavi, I. 2022, ApJ, 937, 75
Astropy Collaboration, Price-Whelan, A. M., Sipőcz, B. M., et al. 2018, AJ, 156, 123
Baklanov, P. V., Blinnikov, S. I., & Pavlyuk, N. N. 2005, AstL, 31, 429
Beasor, E. R., Davies, B., Smith, N., et al. 2020, MNRAS, 492, 5994
Bellm, E. C., Kulkarni, S. R., Graham, M. J., et al. 2019, PASP, 131, 018002
Berger, E., Keating, G. K., Margutti, R., et al. 2023, ApJL, 951, L31
Bertin, E., & Arnouts, S. 1996, A&AS, 117, 393
Blagorodnova, N., Neill, J. D., Walters, R., et al. 2018, PASP, 130, 035003
Blinnikov, S., Lundqvist, P., Bartunov, O., Nomoto, K., & Iwamoto, K. 2000, ApJ, 532, 1132
Blinnikov, S., & Sorokina, E. 2004, Ap&SS, 290, 13
Blinnikov, S. I., Eastman, R., Bartunov, O. S., Popolitov, V. A., & Woosley, S. E. 1998, ApJ, 496, 454
Blinnikov, S. I., Röpke, F. K., Sorokina, E. I., et al. 2006, A&A, 453, 229
Boian, I., & Groh, J. H. 2019, A&A, 621, A109
Boian, I., & Groh, J. H. 2020, MNRAS, 496, 1325
Bostroem, K. A., Pearson, J., Shrestha, M., et al. 2023, arXiv:2306.10119
Bradley, L., Sipőcz, B., Robitaille, T., et al. 2022, astropy/photutils: v1.5.0, Zenodo, doi:10.5281/zenodo.6825092
Breeveld, A. A., Landsman, W., Holland, S. T., et al. 2011, in AIP Conf. Ser. 1358, Gamma Ray Bursts 2010, ed. J. E. McEnery, J. L. Racusin, & N. Gehrels (Melville, NY: AIP), 373
Brown, P. J., Breeveld, A. A., Holland, S., Kuin, P., & Pritchard, T. 2014, Ap&SS, 354, 89
Brown, T. M., Baliber, N., Bianco, F. B., et al. 2013, PASP, 125, 1031
Buchhave, L. A., Bakos, G. Á., Hartman, J. D., et al. 2010, ApJ, 720, 1118
Chambers, K. C., Magnier, E. A., Metcalfe, N., et al. 2016, arXiv:1612.05560
Chevalier, R. A. 2017, in Handbook of Supernovae, ed. R. A. Chevalier & C. Fransson (Berlin: Springer), 875
Chevalier, R. A., & Fransson, C. 1994, ApJ, 420, 268
Chufarin, V., Potapov, N., Ionov, I., et al. 2023, TNSAN, 150, 1
Davies, B., Plez, B., & Petrault, M. 2022, MNRAS, 517, 1483
De, K., Hankins, M. J., Kasliwal, M. M., et al. 2020, PASP, 132, 025001
de Vaucouleurs, G., de Vaucouleurs, A., Corwin, H. G. J., et al. 1991, Third Reference Catalogue of Bright Galaxies (New York: Springer)
Dessart, L., Hillier, D. J., & Audit, E. 2017, A&A, 605, A83
Fabricant, D., Cheimets, P., Caldwell, N., & Geary, J. 1998, PASP, 110, 79
Fan, Z., Wang, H., Jiang, X., et al. 2016, PASP, 128, 115005
Filippenko, A. V., Zheng, W., & Yang, Y. 2023, TNSAN, 123, 1
Fitzpatrick, E. L. 1999, PASP, 111, 63
Flewelling, H. A., Magnier, E. A., Chambers, K. C., et al. 2020, ApJS, 251, 7
Foreman-Mackey, D., Hogg, D. W., Lang, D., & Goodman, J. 2013, PASP, 125, 306
Förster, F., Moriya, T. J., Maureira, J. C., et al. 2018, NatAs, 2, 808
Fulton, M. D., Nicholl, M., Smith, K. W., et al. 2023, TNSAN, 124, 1
Gal-Yam, A., Arcavi, I., Ofek, E. O., et al. 2014, Natur, 509, 471
Goldberg, J. A., & Bildsten, L. 2020, ApJL, 895, L45
Goldberg, J. A., Bildsten, L., & Paxton, B. 2019, ApJ, 879, 3
Goldman, S. R., van Loon, J. T., Zijlstra, A. A., et al. 2017, MNRAS, 465, 403
Gomez, S., Berger, E., Blanchard, P. K., et al. 2020, ApJ, 904, 74
Gomez, S., Berger, E., Blanchard, P. K., et al. 2023, ApJ, 949, 114
Graham, M. J., Kulkarni, S. R., Bellm, E. C., et al. 2019, PASP, 131, 078001
Grefenstette, B. W., Brightman, M., Earnshaw, H. P., Harrison, F. A., & Margutti, R. 2023, ApJL, 952, L3
Haynie, A., & Piro, A. L. 2021, ApJ, 910, 128
Hiramatsu, D., Howell, D. A., Moriya, T. J., et al. 2021, ApJ, 913, 55
Hiramatsu, D., Howell, D. A., Van Dyk, S. D., et al. 2021, NatAs, 5, 903
Hiramatsu, D., Matsumoto, T., Berger, E., et al. 2023, arXiv:2305.11168
Hosseinzadeh, G., Farah, J., Shrestha, M., et al. 2023, ApJL, 953, L16
Howell, D. A. & Global Supernova Project 2017, AAS Meeting Abstracts, 230, 318.03
Hu, N., Wang, E., Lin, Z., et al. 2018, ApJ, 854, 68
Hunter, J. D. 2007, CSE, 9, 90
Itagaki, K. 2023, TNSTR, 2023-1158, 1
Jacobson-Galán, W. V., Dessart, L., Jones, D. O., et al. 2022, ApJ, 924, 15
Jacobson-Galan, W. V., Dessart, L., Margutti, R., et al. 2023, arXiv:2306.04721
Jencson, J. E., Pearson, J., Beasor, E. R., et al. 2023, ApJL, 952, L30
Johnson, S. A., Kochanek, C. S., & Adams, S. M. 2018, MNRAS, 480, 1696
Kasen, D., & Woosley, S. E. 2009, ApJ, 703, 2205
Khatami, D., & Kasen, D. 2023, arXiv:2304.03360
Kilpatrick, C. D., Foley, R. J., Jacobson-Galán, W. V., et al. 2023, ApJL, 952, L23
Kochanek, C. S., Fraser, M., Adams, S. M., et al. 2017, MNRAS, 467, 3347
Koltenbah, B. 2023, TNSAN, 144, 1
Kozyreva, A., Nakar, E., & Waldman, R. 2019, MNRAS, 483, 1211
Kuriyama, N., & Shigeyama, T. 2020, A&A, 635, A127
Landolt, A. U. 1983, AJ, 88, 439
Landolt, A. U. 1992, AJ, 104, 340
Lang, D. 2014, AJ, 147, 108
Lundquist, M., O'Meara, J., & Walawender, J. 2023, TNSAN, 160, 1
Mainzer, A., Bauer, J., Cutri, R. M., et al. 2014, ApJ, 792, 30
Mao, Y., Zhang, M., Cai, G., et al. 2023, TNSAN, 130, 1
Margutti, R., Milisavljevic, D., Soderberg, A. M., et al. 2014, ApJ, 780, 21
Masci, F. J., Laher, R. R., Rusholme, B., et al. 2019, PASP, 131, 018003
Masci, F. J., Laher, R. R., Rusholme, B., et al. 2023, arXiv:2305.16279
Matsumoto, T., & Metzger, B. D. 2022, ApJ, 936, 114
Matthews, D., Margutti, R., AJ, N., et al. 2023, ATel, 16091, 1
Matzner, C. D., & McKee, C. F. 1999, ApJ, 510, 379
McCully, C., Turner, M., Volgenau, N., et al. 2018, LCOGT/banzai: Initial Release, v0.9.4, Zenodo, doi:10.5281/zenodo.1257560
Meisner, A. M., Lang, D., & Schlegel, D. J. 2018, AJ, 156, 69
Mink, D. J. 2011, in ASP Conf. Ser. 442, Astronomical Data Analysis Software and Systems XX, ed. I. N. Evans et al. (San Francisco, CA: ASP), 305
Mink, D. J., Wyatt, W. F., Caldwell, N., et al. 2007, in ASP Conf. Ser. 376, Astronomical Data Analysis Software and Systems XVI, ed. R. A. Shaw, F. Hill, & D. J. Bell (San Francisco, CA: ASP), 249
Mink, D. J., Wyatt, W. F., Roll, J. B., et al. 2005, in ASP Conf. Ser. 347, Astronomical Data Analysis Software and Systems XIV, ed. P. Shopbell, M. Britton, & R. Ebert (San Francisco, CA: ASP), 228
Moriya, T. J., Förster, F., Yoon, S.-C., Gräfener, G., & Blinnikov, S. I. 2018, MNRAS, 476, 2840
Morozova, V., Piro, A. L., Fuller, J., & Van Dyk, S. D. 2020, ApJL, 891, L32
Morozova, V., Piro, A. L., Renzo, M., et al. 2015, ApJ, 814, 63
Morozova, V., Piro, A. L., & Valenti, S. 2018, ApJ, 858, 15
Nakar, E., & Sari, R. 2010, ApJ, 725, 904
Neustadt, J. M. M., Kochanek, C. S., & Rizzo Smith, M. 2023, arXiv:2306.06162
Ofek, E. O., Sullivan, M., Cenko, S. B., et al. 2013, Natur, 494, 65
Ofek, E. O., Sullivan, M., Shaviv, N. J., et al. 2014, ApJ, 789, 104
Oliphant, T. E. 2006, A Guide to NumPy (USA: Trelgol Publishing)
Paxton, B., Bildsten, L., Dotter, A., et al. 2011, ApJS, 192, 3
Paxton, B., Cantiello, M., Arras, P., et al. 2013, ApJS, 208, 4
Paxton, B., Marchant, P., Schwab, J., et al. 2015, ApJS, 220, 15

Paxton, B., Schwab, J., Bauer, E. B., et al. 2018, ApJS, 234, 34
Paxton, B., Smolec, R., Schwab, J., et al. 2019, ApJS, 243, 10
Perley, D. A., Gal-Yam, A., Irani, I., & Zimmerman, E. 2023, TNSAN, 119, 1
Perley, D. A., & Irani, I. 2023, TNSAN, 120, 1
Piascik, A. S., Steele, I. A., Bates, S. D., et al. 2014, Proc. SPIE, 9147, 91478H
Piro, A. L. 2015, ApJL, 808, L51
Piro, A. L., Haynie, A., & Yao, Y. 2021, ApJ, 909, 209
Pledger, J. L., & Shara, M. M. 2023, ApJL, 953, L14
Popov, D. V. 1993, ApJ, 414, 712
Poznanski, D., Prochaska, J. X., & Bloom, J. S. 2012, MNRAS, 426, 1465
Riess, A. G., Yuan, W., Macri, L. M., et al. 2022, ApJL, 934, L7
Schlafly, E. F., & Finkbeiner, D. P. 2011, ApJ, 737, 103
Science Software Branch at STScI (2012) PyRAF: Python Alternative for IRAF, Astrophysics Source Code Library, ascl:1207.011
SDSS Collaboration, Albareti, F. D., Allende Prieto, C., et al. 2017, ApJS, 233, 25
Sgro, L. A., Esposito, T. M., Blaclard, G., et al. 2023, RNAAS, 7, 141
Shingles, L., Smith, K. W., Young, D. R., et al. 2021, TNSAN, 7, 1
Singh Teja, R., Singh, A., Dutta, A., et al. 2023, ApJL, 954, L12
Smartt, S. J. 2009, ARA&A, 47, 63
Smartt, S. J. 2015, PASA, 32, e016
Smith, K. W., Smartt, S. J., Young, D. R., et al. 2020, PASP, 132, 085002
Smith, N., Pearson, J., Sand, D. J., et al. 2023, arXiv:2306.07964
Soraisam, M. D., Szalai, T., Van Dyk, S. D., et al. 2023, arXiv:2306.10783
Steele, I. A., Smith, R. J., Rees, P. C., et al. 2004, Proc. SPIE, 5489, 679
Stritzinger, M., Valerin, G., Elias-Rosa, N., et al. 2023, TNSAN, 145, 1
Strotjohann, N. L., Ofek, E. O., Gal-Yam, A., et al. 2021, ApJ, 907, 99
Sukhbold, T., Ertl, T., Woosley, S. E., Brown, J. M., & Janka, H. T. 2016, ApJ, 821, 38
Svirski, G., Nakar, E., & Sari, R. 2012, ApJ, 759, 108
Szentgyorgyi, A. H., Cheimets, P., Eng, R., et al. 1998, Proc. SPIE, 3355, 242
Szentgyorgyi, A. H., & Furész, G. 2007, in The 3rd Mexico-Korea Conference on Astrophysics: Telescopes of the Future and San Pedro Mártir, Revista Mexicana de Astronomía y Astrofísica, ed. S. Kurtz et al., 28 (Serie de Conferencias), 129
Szentgyorgyi, A. H., Geary, J. G., Latham, D. W., et al. 2005, AAS Meeting Abstracts, 207, 110.10
Takei, Y., Tsuna, D., Kuriyama, N., Ko, T., & Shigeyama, T. 2022, ApJ, 929, 177
Teja, R. S., Anupama, G., Sahu, D., Kurre, M., & Pramod 2023, TNSCR, 2023-123, 1
Terreran, G., Jacobson-Galán, W. V., Groh, J. H., et al. 2022, ApJ, 926, 20
Tokarz, S. P., & Roll, J. 1997, in ASP Conf. Ser. 125, Astronomical Data Analysis Software and Systems VI, ed. G. Hunt & H. Payne (San Francisco, CA: ASP), 140
Tonry, J. L., Denneau, L., Heinze, A. N., et al. 2018, PASP, 130, 064505
Tsang, B. T. H., Kasen, D., & Bildsten, L. 2022, ApJ, 936, 28
Tsuna, D., Murase, K., & Moriya, T. J. 2023, ApJ, 952, 115
Tsuna, D., Takei, Y., Kuriyama, N., & Shigeyama, T. 2021, PASJ, 73, 1128
Tsuna, D., Takei, Y., & Shigeyama, T. 2023, ApJ, 945, 104
UnWISE Team 2021, unWISE Catalog, IPAC, doi:10.26131/IRSA525
Valenti, S., Howell, D. A., Stritzinger, M. D., et al. 2016, MNRAS, 459, 3939
VanDyk, S. D. 2017, in Handbook of Supernovae, ed. A. W. Alsabt & P. Murdin (Berlin: Springer), 693
Vasylyev, S. S., Yang, Y., Filippenko, A. V., et al. 2023, arXiv:2307.01268
Virtanen, P., Gommers, R., Oliphant, T. E., et al. 2020, NatMe, 17, 261
Wang, S., & Chen, X. 2019, ApJ, 877, 116
Waskom, M., Botvinnik, O., Ostblom, J., et al. 2020, mwaskom/seaborn: v0.10.0 (January 2020), v0.10.0, Zenodo, doi:10.5281/zenodo.3629446
Wright, E. L., Eisenhardt, P. R. M., Mainzer, A. K., et al. 2010, AJ, 140, 1868
Yamanaka, M., Fujii, M., & Nagayama, T. 2023, PASJ, Advance Access
Yaron, O. 2023, TNSCR, 2023-126, 1
Yaron, O., Perley, D. A., Gal-Yam, A., et al. 2017, NatPh, 13, 510
Yoon, S.-C., & Cantiello, M. 2010, ApJL, 717, L62
Zacharias, N., Finch, C. T., Girard, T. M., et al. 2013, AJ, 145, 44
Zackay, B., Ofek, E. O., & Gal-Yam, A. 2016, ApJ, 830, 27
Zhang, Y., Fan, Z., Zheng, J., Zhang, J., & He, M. 2023, TNSAN, 132, 1